

pubs.acs.org/JACS Article

# Two-Legged Molecular Walker and Curvature: Mechanochemical Ring Migration on Graphene

Sayan Banerjee, Nathaniel Hawthorne, James D. Batteas, and Andrew M. Rappe\*



Cite This: J. Am. Chem. Soc. 2023, 145, 26765-26773



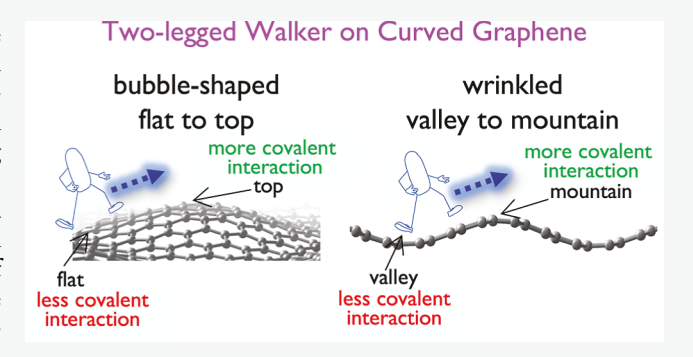
**ACCESS** 

Metrics & More

Article Recommendations

Supporting Information

ABSTRACT: Attaining controllable molecular motion at the nanoscale can be beneficial for multiple reasons, spanning from optoelectronics to catalysis. Here we study the movement of a two-legged molecular walker by modeling the migration of a phenyl aziridine ring on curved graphene. We find that directional ring migration can be attained on graphene in the cases of both 1D (wrinkled/rippled) and 2D (bubble-shaped) curvature. Using a descriptor approach based on graphene's frontier orbital orientation, we can understand the changes in binding energy of the ring as it translates across different sites with variable curvature and the kinetic barriers associated with ring migration. Additionally, we show that the extent of covalent bonding between



graphene and the molecule at different sites directly controls the binding energy gradient, propelling molecular migration. Importantly, one can envision such walkers as carriers of charge and disruptors of local bonding. This study enables a new way to tune the electronic structure of two-dimensional materials for a range of applications.

## ■ INTRODUCTION

Performing directional and controlled translational and rotational motion of molecules has been an active area of research because of its immediate application in areas spanning from energy conversion and optoelectronics to molecular aggregation and catalysis. 1-6 A set of strategies has been developed to realize controllable molecular motion at the atomic scale. This includes the rational tailoring of chemical interactions to synthesize chemical motifs, e.g., molecular shuttles, 7,8 nanocars, 9,10 and molecular walkers, 11,12 as well as harnessing geometric effects to direct molecular migration.<sup>1</sup> To this end, the selection of a support or platform with which one can perform such motions can provide an additional design dimension to work with. In this context, twodimensional materials (2D) offer a unique opportunity, due to their control over atomically precise synthetic protocols and accurate characterization. 14-21 Molecular migration on graphene has been realized experimentally, and molecular motion has been shown to depend on the electronic nature of the molecular functional groups present, i.e., electron-donating vs electron-withdrawing groups.

Previous reports show that mechanical perturbations, such as strain and curvature of 2D materials, can be realized experimentally using state-of-the-art methods. The use of mechanical distortion provides an alternate avenue to perform chemical reactions apart from thermal, photochemical, or electrochemical approaches. Furthermore, mechanochemistry enables one to realize novel chemical processes and perform directed chemical syntheses on 2D materials. Recently, we

have demonstrated that directional molecular motion can be attained on graphene by exploiting mechanical distortions. <sup>13</sup> In that study, an aromatic molecule bound to graphene by one C–C bond has been shown to migrate from regions of positive curvature (valley) to regions of negative curvature (mountain) on sinusoidally curved graphene. We denoted this system a one-legged walker as there is only a single bond between the molecule and the graphene at any given time as the molecule migrates. Interestingly, for noncovalent interactions, we have recently shown that these prefer motions opposite to covalent systems, with mechanical distortions driving molecular motion from the mountain regions to the valley regions on curved graphene. <sup>44</sup>

Moving beyond these studies, we have now designed and investigated a two-legged walker, where two bonds migrate in tandem, one after another. This can be realized by bonding a terminal N group across the C=C bond network of graphene, forming an aziridine ring,<sup>45-51</sup> with individual molecule—graphene bonds breaking and reforming as the molecule moves. This class of functionalization has been reported to locally open a band gap in graphene,<sup>48,52</sup> and therefore it

Received: August 14, 2023 Revised: November 8, 2023 Accepted: November 13, 2023 Published: December 4, 2023





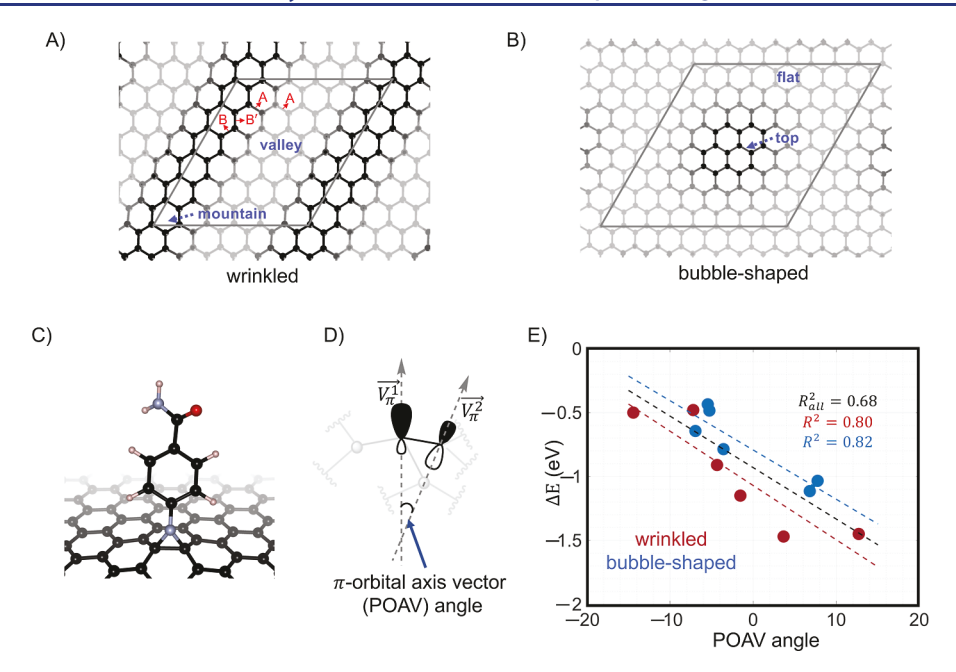


Figure 1. Aziridine ring formation on graphene. (A) Wrinkled/rippled graphene as a representative system for 1-dimensional curvature. Three types of C=C bonds are present, bonds along the uphill directions (A) and bonds at angle (B, B'). (B) Bubble-shaped graphene as a representative system for 2-dimensional curvature. (C) Studied three-membered aziridine ring, 4-carboxamide phenyl aziridine, was a two-legged walker. (D) Schematic showing the  $\pi$ -orbital axis vector (POAV) angle. (E) Correlation between the POAV angle and the binding energy of the aziridine ring. The linear fits for wrinkled (red lines) and bubbled graphene (blue lines) individually and for both of them together (black lines) are shown as dotted lines. The atomic color code is C (black), H (white), O (red), and N (light blue).

provides a way to tailor nanomaterials for optoelectronic purposes.<sup>53</sup> Migration of a functionalized center on graphene provides a way to spatially control the local frontier energy levels as well as the carrier (electron/hole) concentrations and defect states. Moreover, understanding how a ring moves on curved graphene can be crucial for driving cyclization reactions and facilitating the movement of such rings on curved graphene, which has been a key area of interest. 54-56 Herein, we demonstrate through density functional theory (DFT) calculations that directional ring migration of a two-legged walker (4-carboxamide phenyl aziridine) can be induced on graphene via control of the curvature effect. We first show that ring migration can be generalized across different graphene structures encompassing one-dimensional (1D, wrinkled) and two-dimensional (2D, bubble-shaped) curvatures; we discuss this process as mechanochemical ring migration. Furthermore, we apply a descriptor approach based on the graphene orbital orientation at the functionalized centers to understand the thermodynamic stabilization of the rings across different curvature types. We then established the atomistic and electronic origins of the trends observed in the kinetic barriers of ring migration. The results illustrate that curvature in 2D materials can be used to direct the motion of a two-legged walker, providing a dynamic way to control the carrier concentration and defect states of 2D materials via their bonding location.

## ■ RESULTS AND DISCUSSION

Binding Energy of Aziridine on Graphene. We have considered two different graphene geometries, wrinkled (Figure 1A) and bubbled (Figure 1B), as representative systems for 1D and 2D curvature, respectively, to study the migration of a two-legged walker on a 2D platform. Experimentally, both 1D curvature and 2D curvature of 2D

materials have been realized.  $^{30,57-68}$  For wrinkled (Figure 1A) graphene, 1/R = 0.06 Å $^{-1}$ , and for bubbled (Figure 1B) graphene, 1/R = 0.04 Å $^{-1}$ , are considered, where R is the radius of curvature, and such curvatures have been realized experimentally.  $^{30,64-67}$  We note that changing R can affect the relative energetics, although the trends are expected to remain the same. Hence, the migration of aziridine can have dynamic (spatiotemporal) effects on carrier and defect properties. Accordingly, we consider an aziridine ring (Figure 1C) as a model two-legged walker on graphene. The details of the DFT calculations are given in the computational details section.

We first focus on understanding the binding energy of an aziridine ring  $(\Delta E)$  on different sites of wrinkled and bubbled graphene. In general, we find that for wrinkled graphene (Figure 1A), the mountain sites have stronger binding energy than the valley sites, and for bubbled graphene, the top sites have stronger binding energy than the flat sites (Figure 1B). To understand the binding energy trend, we first apply the  $\pi$ orbital axis vector (POAV)-based descriptor. 69-72 POAV can capture the orientations of orbitals for nonplanar conjugated organic molecules, and a similar situation can be envisioned for functionalized graphene. Here, we use the POAV approach to find the orientation of the out-of-plane  $2p_z$  orbitals, the frontier orbitals of graphene. The angle between two POAVs is defined as the POAV angle (Figure 1D) and has been reported previously to explain the barrier trends of a single C-C bond migration.<sup>13</sup> We extend the POAV angle descriptor for ring binding on graphene and find that the POAV angle between the two C atoms of graphene is correlated with the  $\Delta E$  (Figure 1E) of aziridine binding across that C=C bond. In other words, given the POAV angle of the unfunctionalized curved graphene, the  $\Delta E$  of aziridine binding can be predicted. We find that when the POAV angle is positive, graphene-aziridine binding is stronger, wherein negative POAV corresponds to a

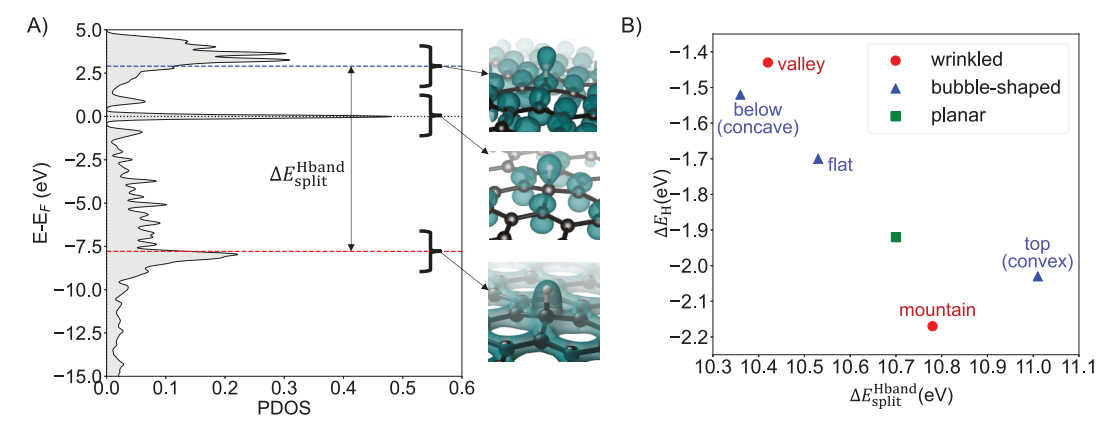


Figure 2. Graphene—adsorbate interaction. (A) Projected density of states of H adsorbed on planar flat graphene. Black dotted line corresponds to the Fermi energy, and red and blue dotted lines correspond to the center of the H band below and above Fermi energy, respectively. The integrated local density of states (ILDOS) for different energy regions is shown on the right. Note that ILDOS plots also have contributions from graphene orbitals. (B) H band split ( $\Delta E_{\rm split}^{\rm H band}$ ) vs H binding energy ( $\Delta E_{\rm H}$ ) is shown for planar (flat), wrinkled, and bubble-shaped graphene.  $\Delta E_{\rm H}$  is calculated relative to an isolated H atom.

weaker interaction (Figure 1E). This is in line with previous findings from our groups, showing that positive POAV angle regions (such as mountains) are more prone to out-of-plane functionalization and have stronger covalent binding with an adsorbate. This is due to the fact that the functionalization of graphene C=C causes pyramidalization and out-of-plane distortion of the graphene C. Therefore, regions that are closer to pyramidal geometry, that is, the regions with positive POAV angle, can offer a stronger binding.

To understand the origin of the covalent bond strength at different regions of the curved graphene, we study H adsorption as a model system. We focus on understanding the extent of covalent binding when only one orbital is involved from the adsorbate, here 1s of H, and correlate these results with the POAV angle descriptor findings described in the previous paragraph. We find that for a C–H bond formation on graphene, three different regions appear in the projected density of state (PDOS) plot (Figure 2A), bonding, nonbonding, and antibonding regions, in accordance with the previous observation. We calculate the center of the H band below the Fermi energy (red dotted lines in Figure 2A) and above the Fermi energy (blue dotted line in Figure 2A) and define it as the H band split ( $\Delta E_{\rm solit}^{\rm H\,band}$  in Figure 2A).

$$\Delta E_{\text{split}}^{\text{H band}} = \frac{\int_{E_{\text{F}}}^{\infty} \rho_{1s}(E)E \, dE}{\int_{E_{\text{F}}}^{\infty} \rho_{1s}(E) \, dE} - \frac{\int_{-\infty}^{E_{\text{F}}} \rho_{1s}(E)E \, dE}{\int_{-\infty}^{E_{\text{F}}} \rho_{1s}(E) \, dE}$$
(1)

Therefore, a higher value of  $\Delta E_{\rm split}^{\rm H\ band}$  corresponds to a higher extent of covalent interaction via orbital hybridization. We find that the mountain region has a higher  $\Delta E_{\rm split}^{\rm H\ band}$  than the valley region in wrinkled graphene. Similarly, the top convex region (top of the bubble) has a higher  $\Delta E_{\rm split}^{\rm H\ band}$  than the concave underside (opposite to top of the bubble) and flat regions in bubble-shaped graphene. Figure 2B shows that such a higher  $\Delta E_{\rm split}^{\rm H\ band}$  corresponds to stronger covalent interaction with H, resulting in more favorable H binding energy ( $\Delta E_{\rm H}$ ). The higher  $\Delta E_{\rm split}^{\rm H\ band}$  (stronger covalent interaction) at the bottom of the wrinkled graphene and the top of the bubble-shaped graphene indicates a higher extent of available electron

density for covalent bond formation. In other words, regions with a positive POAV angle have higher  $\Delta E_{\rm split}^{\rm H\ band}$  than regions with negative and zero POAV angles due to higher orbital interaction, explaining the origin of differential binding energy. Note that the  $\Delta E_{\rm H}$  for the flat region of bubble-shaped graphene and for no curvature, flat graphene are slightly different. This happens because of the sp³ distortion due to the C–H bond near a bubble, which does not exist for planar flat graphene. Therefore, we confirm that closer to the pyramidalization geometry, covalent bond strength increases due to the increased orbital interaction (higher extent of available electron density) with H. The same model can be applied to explain the binding energy trends when many orbital interactions are involved, such as phenyl aziridine in Figure 1C,E.

Hence, we show that the POAV angle descriptor can help us understand the binding energy trend in both wrinkled (red markers in Figure 1E) and bubbled (blue markers in Figure 1E) graphene. Note that we observe a relatively higher amount of scatter in binding energy vs POAV for wrinkled graphene, which can be a consequence of the different orientations observed for the aziridine ring (vide infra). Using H as a model adsorbate, we then confirm that regions with a positive POAV angle offer stronger bond formation due to the higher extent of orbital interaction. This confirms the generalizability of the proposed POAV angle descriptor to understand the binding energy trends. Furthermore, this suggests that the aziridine ring binding energy is dictated by the immediate local environment, as the binding energy for graphene with different curvatures can be predicted and understood using a descriptor featuring only the local environment. Overall, the results illustrate that there is a binding energy gradient depending on the local geometry of the wrinkled and bubbled graphene. Moreover, because aziridine is bound to the two nearest-neighbor carbons, this gradient should strongly dictate the direction of aziridine migration based on curvature. Furthermore, to understand the generalizability of the thermodynamic drive toward mountain sites (wrinkled graphene) and top sites (bubble-shaped graphene), we examine epoxide, aziridine, and cyclopropane rings. Additionally, we vary the nature of the functional group at the para position of the aryl adsorbate. We find that the thermodynamic drive exists across ring types, and

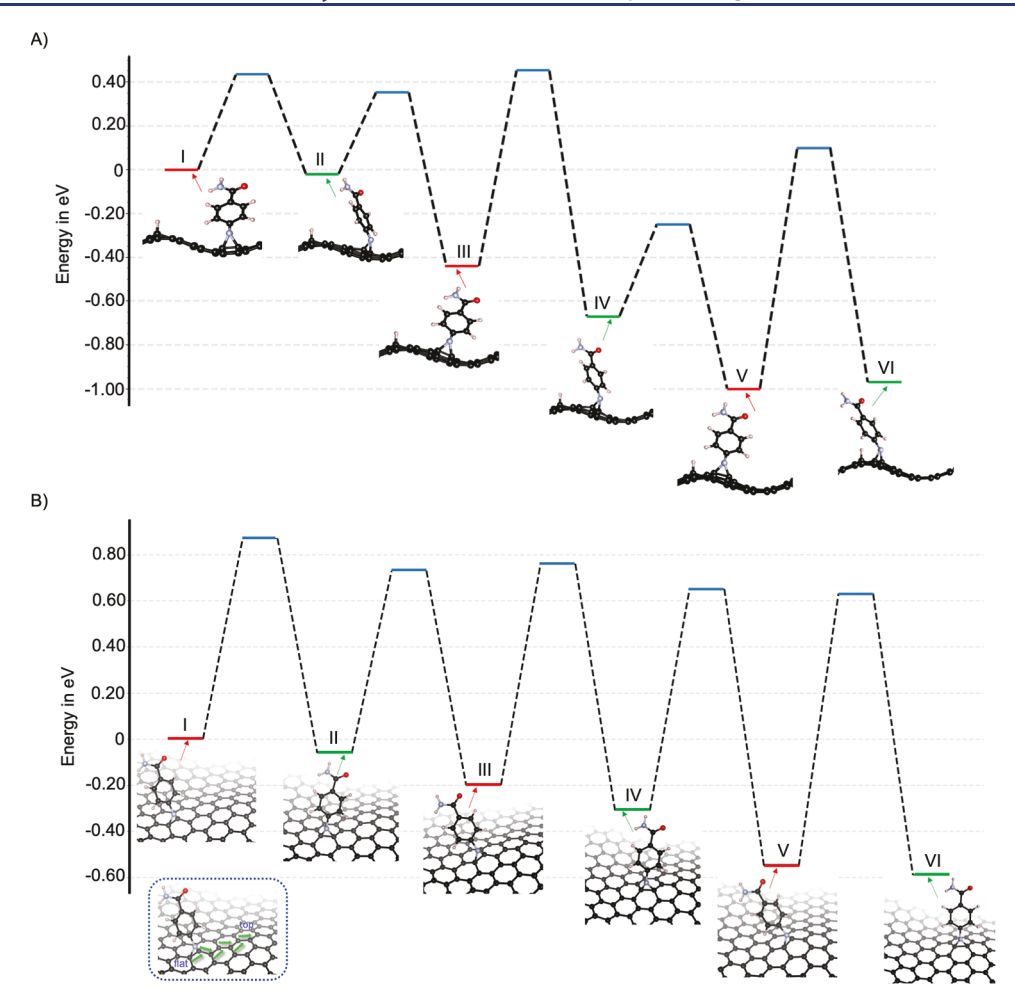


Figure 3. Two-legged molecular walker on graphene. (A) Ring migration on wrinkled/rippled graphene as a result of one-dimensional curvature. Blue lines represent transition states, and red and green lines correspond to intermediates with different molecular orientations. Co-adsorbed —H is included to stabilize the sinusoidal curvature of graphene. (B) Ring migration on bubble-shaped graphene as a result of two-dimensional curvature. The direction considered is shown in the inset by using green arrows. Blue lines correspond to transition states, and red and green lines correspond to the intermediates with different molecular orientation. The atomic color code is C (black), H (white), O (red), and N (light blue).

further details are provided in the Supporting Information (Figure S6). To explore this, in the next section, we investigate whether there is also a kinetically feasible pathway to move to the lowest energy sites in order to achieve mechanochemically driven two-legged walker on curved graphene.

Kinetics of Ring Migration. After establishing the binding energy trend, we now focus on understanding the kinetics of ring migration in wrinkled and bubbled graphene. The ring migration here is defined as the motion of the aziridine ring N attachment from one C=C bond of graphene (which becomes C-C as a result of functionalization) to the adjacent C=C. Since we envision including curvature to perform such migration, we view these events as mechanochemical ring migration. Here the ring migration pathway is considered from the valley to the mountain on a wrinkled graphene (Figures 1A and 3A) and ring migration from the flat region to the top of a bubble in graphene (Figures 1B and 3B).

First, we establish ring migration on (1D) wrinkled graphene. Unlike the migration of a single-legged walker, <sup>13</sup> we do not observe a linear change in ring migration barrier as it moves from the valley toward the mountain. We find that there are two different orientations for the bound aziridine ring, along A and B graphene C=C, respectively, as represented in Figure 1A. Those different orientations are depicted using the

red and green lines in Figure 3A. The chemisorption energies for each orientation separately follow a linear trend<sup>13</sup> as the ring moves toward the mountain. In addition, as the molecule moves to more stable sites, the ring migration barrier also increases. For example, for the pathway connecting intermediates I-III-V in Figure 3A, I-III has a lower kinetic barrier than III-V, where the barrier refers to the highest transition-state energy (blue lines) connecting the intermediates. The same trend is followed for the migration pathway connecting II-IV-VI in Figure 3A. Therefore, we have investigated the spatial pathway of how directional ring migration can happen from the valley regions to the mountain regions on wrinkled graphene. It is worth noting that the ring walker follows the direction of higher electron density as it moves from the valley to the mountain sites on the wrinkled graphene. In other words, the walker moves at each step to achieve a higher extent of covalent binding, which occurs due to the greater available electron density near the mountain regions, as shown in Figure 2B.

We now focus on the ring migration kinetics for (2D) bubble-shaped graphene. Here, the ring migration is studied from the flat to the top of the bubble (Figure 1A) as shown by the green arrows in the inset of Figure 3B. We find two different sets of orientations of the aziridine on graphene, (I,

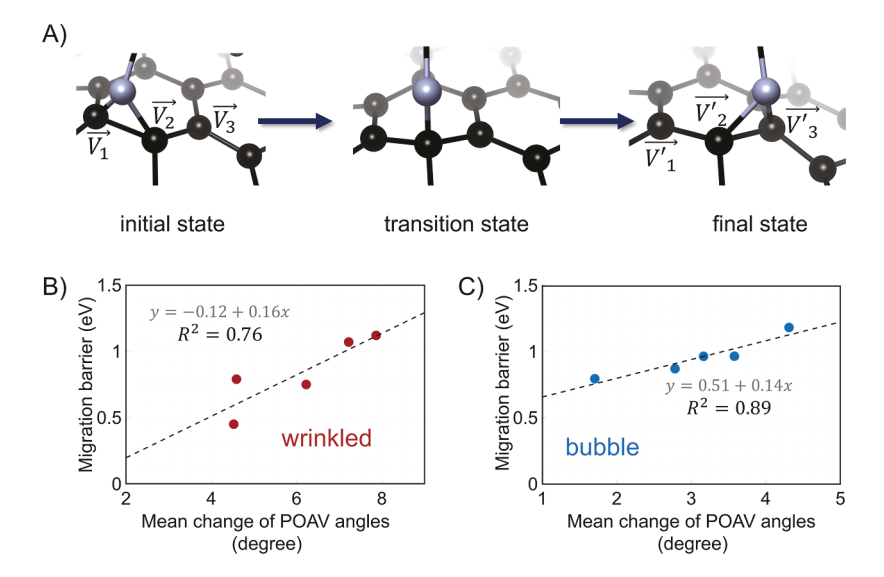


Figure 4. Understanding the kinetic barrier trends. (A) Schematic showing the migration of the two-legged aziridine ring (two C-N bonds) via a one-legged transition state. POAV at each participating C atom in the initial and final states are labeled. (B) Correlation between mean POAV angle and kinetic barrier of ring migration on wrinkled graphene. (C) Correlation between mean POAV angle and kinetic barrier of ring migration on bubble-shaped graphene. Mean absolute change of the POAV angles is defined as  $\frac{1}{3}\sum_{i< j} \overrightarrow{|V_i \cdot V_j|} - \overrightarrow{V_i' \cdot V_j'}$ . The atomic color code is C (black), N (light blue).

III, V) and (II, IV, VI) in Figure 3B, resembling the binding geometries in Figure 3A. We find the same migration barrier trend as observed in wrinkled graphene; two different sets of intermediates (red and green lines in Figure 3B) follow the increasing migration barrier trend as the ring gains thermodynamic stability. Hence, we demonstrate that for bubble-shaped graphene also one can attain directional migration from the flat regions to the bubble top regions. Similar to the migration pathway on the wrinkled graphene, it is important to highlight that the ring walker traces the path of heightened electron density while it transitions from the flat to the top sites on the bubble-shaped graphene. As previously mentioned (refer to Figure 2B), this phenomenon is a consequence of the increased electron density in the vicinity of the top convex regions on the bubble-shaped graphene. We note different patterns for the two-legged molecular walker in the two different cases (Figure 3), such as a relatively more linear change in energetics for bubbled graphene than wrinkled graphene and relatively higher migration barriers for bubbled graphene. As the curvature affects the C=C bonds in different ways (A, B, and B' in Figure 1A and uniform orientation in Figure 1B), such a geometric effect can also influence the relative ring migration energetics. It is worth noting that the two orientations mentioned above for Figure 3 are also a consequence of how the curvature direction affects the C=C bonds in both wrinkled and bubble-shaped graphene. Therefore, the distinct energy trends can be traced back to the different nature and amount of curvature involved (1D vs 2D curvature) for the two cases, although we do not focus on the quantitative trends between the two curvature scenarios in this work.

Overall, in this section, we show that directional ring migration can be attained using the thermodynamic drive and related kinetic feasibility for both wrinkled (1D) and bubbled (2D) graphene. Furthermore, Boltzmann population analyses show that the walkers will be nearly corralled to the mountain and top sites of the wrinkled and bubble-shaped graphene,

respectively, at room temperature or at any lower or moderately elevated temperature, confirming the directional ring migration trend on curved graphene (Figure S5). In the next section, we focus on understanding the atomistic origin of the kinetic barrier trends, i.e., why the kinetic barrier depends on the orientation of the aziridine and why kinetic barriers can be different as one varies the type and amount of curvature.

Understanding the Kinetic Barrier Trends of Ring **Migration.** In this section, we seek to understand the kinetic trends observed in ring migration on wrinkled and bubbleshaped graphene by using a descriptor-based approach. As outof-plane functionalization requires the participation of graphene 2pz orbitals, we focus on the graphene 2pz frontier orbital orientation and how the orientations of the participating orbitals change as the molecule migrates. Here, we apply the POAV method<sup>69-72</sup> to quantify the orbital reorientation. In the case of migration of a C-C bond on graphene, it has been shown that the angle between two POAVs (Figure 1D) can explain the migrational barriers. 13 As shown in Figure 4A, two-legged ring migration happens via a one-legged transition state (middle panel in Figure 4A). Ring migration directly involves three carbon atoms (the two that it is currently bonded to plus the one it is moving toward, Figure 4A); thus we consider the POAV of three C centers  $(V_1, V_2, V_3)$ and  $V_3$ ), unlike the migration of one C–C bond, where two C centers sufficed. 13 The three POAVs in the initial state are  $\overline{V_{11}}$  $\overrightarrow{V_2}$ , and  $\overrightarrow{V_3}$ , and the three POAVs in the final state are  $\overrightarrow{V_1}$ ,  $\overrightarrow{V_2}$ , and  $V_3'$  (Figure 4A).

Three POAVs in both the initial and final states allow us to define three angles between the vector pairs in each state. The angles directly quantify the amount of  $2p_z$  orbital reorientation at the three carbon centers involved in migration. The change in the angles between the initial and final states should capture the relative amount of orbital orientation involved in the ring

migration step. To be specific, we consider the POAV angle differences between  $V_1 \cdot V_2$  and  $V_1' \cdot V_2'$ ,  $V_1 \cdot V_3$  and  $V_1' \cdot V_3'$ , and  $\overrightarrow{V_2} \cdot \overrightarrow{V_3}$  and  $\overrightarrow{V_2} \cdot \overrightarrow{V_3}$ . We find that the mean absolute change in the POAV angles, which can be expressed as  $\frac{1}{3}\sum_{i < j} |\overrightarrow{V_i} \cdot \overrightarrow{V_j} - \overrightarrow{V_i'} \cdot \overrightarrow{V_j'}|$  (mean change of POAV angle in Figure 4B,C), can explain the migration barrier trend (Figure 4B,C) for both the wrinkled and bubble-shaped graphene. We find that the  $R^2$  values are 0.76 and 0.89, respectively, for wrinkled and bubble-shaped graphene, confirming the validity of the descriptor. The change in POAV angles represents the extent of orbital rearrangement involved in the ring migration step at the three participating carbon centers. Note that the descriptor helps explain the importance of the frontier orbitals which have out-of-plane orientations, in the in-plane migration process. So, a higher value of mean POAV angle change indicates that more 2pz frontier orbital reorientation is involved in that step, resulting in a higher migration barrier. We find that for both wrinkled and bubbled graphene, higher orbital reorientation entails a higher migration barrier (Figure 4B,C). This is chemically intuitive, since the orbitals first need to reorient to attain the one-legged transition state and then need to reorient further to attain the ground-state structure of the next intermediate of the migration pathway (Figure 4A). Therefore, we show that the feasibility of the migration process is controlled by the orbital reorientation required going from the initial state to the final state. Furthermore, it is worth mentioning that the descriptor derived from the ground-state aziridine-functionalized graphene geometries can capture the kinetic barrier trends reasonably well. Note that the absolute change in mean POAV angle is different for wrinkled and bubbled graphene (x axis in Figure 4B,C), which can be traced back to the variable nature and amount of the curvature involved (1D vs 2D curvature) as discussed before. To be specific, the relative orientation of the C=C bonds with respect to the migration direction in the two different cases (such as A, B, and B' for wrinkled graphene and the uniform orientation of the C=C bonds for bubble-shaped graphene in Figure 1) can affect the absolute values of the descriptor. Also, we conjecture that the different orientations of the walker, which have a more pronounced effect on the ring migration kinetics for wrinkled graphene (Figure 3A), can lead to some scatter in Figure 4B.

Overall, we find that the amount of  $2p_z$  orbital reorientation involved in the migration step at the three C centers is quantitatively correlated with the ring migration barrier. Furthermore, we illustrate that the descriptor developed herein can be generalized across different types and values of curvature. Additionally, the descriptor reveals that all three C centers are actively involved in the ring migration step, which is in contrast to the migration of a C–C bond, where a two-centered descriptor could explain the trends. The developed descriptor can further be used to understand how adsorbates migrate on curved 2D materials in general.

Note that the migration energetics reported herein for this particular adsorbate, with a fixed rumple length of graphene, can be further tuned to control the time scale of the migration process. In this regard, varying the rumple length and curvature can be explored to either facilitate or slow down the migration process. Higher rumple length of graphene or lower curvature will lead to a lower POAV angle, resulting in a

lower thermodynamic drive for the migration (Figure 1E). Additionally, it can be conjectured that a lower curvature will also necessitate a smaller change in the  $2p_z$  orbital reorientation for the migration step, leading to reduced migration barriers and consequently faster kinetics (Figure 4). Separately, previous studies have demonstrated that distinct migration trends can be observed for electron-rich and electron-poor walkers. Therefore, by modifying the electronic nature of the ring walker through the substitution of different functional groups in the aziridine ring, the migration kinetics and associated time scale can be further varied. Future studies will focus on exploring these effects to control the migration kinetics and time scale.

Because the barriers are on the order of 1 eV, diffusion occurs on a reasonably fast time scale, enabling experimental demonstrations of this effect at room temperature. Our studies point to the ability to direct molecular migration experimentally as a means of tuning the physicochemical properties of 2D materials. We have previously shown that spatially controlled functionalization of graphene with azides can yield localized scattering of the graphene plasmon,<sup>53</sup> and thus by depositing graphene on patterned substrates with controlled localized curvature, one can envision tracking migration to locations of high localized curvature using spatially resolved vibrational spectroscopies,<sup>22,30</sup> near-field scattering,<sup>53</sup> or high-resolution optical fluorescence measurements.<sup>75</sup>

### CONCLUSIONS

We demonstrate that a two-legged molecular walker can be realized by exploring the effect of graphene curvature on mechanochemically driven diffusion by using a ring migration model. We describe the thermodynamics and kinetics of the ring migration of functionalized phenyl aziridine for different graphene geometries, and we find that the 2pz orbital reorientation involved in the migration step can quantitatively explain the atomistic origin of the ring migration barriers. We derive a descriptor using the ground-state properties of a curved graphene, specifically the angles between the relevant C 2p orbitals, and relate that further to the covalent strength at different regions on curved graphene. Thus, the results provide experimentally tunable and predictable ways to design systems to perform mechanochemical ring migration. As ring migration can also be considered as a dynamical carrier and defect migration, we show that controllable carrier and defect migration and thereby local concentration can be achieved using mechanochemistry. For instance, the electronic nature of the walkers can be adjusted by substituting the para position of the aryl group with various groups (electron-donating/ withdrawing), resulting in the directional movement of electron-rich or electron-poor states. This can potentially provide a new dimension in flexoelectronics and catalysis using 2D materials. The results suggest that more 2D materials can be explored as a platform to attain the directional motion of a two-legged walker, which can provide control over its local electronic structure.

#### COMPUTATIONAL DETAILS

DFT calculations have been performed using the QUANTUM ESPRESSO software package. The climbing image nudged elastic band method is used to calculate the kinetic barriers for the migration. Dimensional curvature is modeled using a  $(6 \times 6)$  supercell of graphene with a  $\Gamma$  centered  $(3 \times 3 \times 1)$  k-

point grid (Figure 1A). 2-Dimensional curvature is modeled using a  $(8 \times 8)$  supercell of graphene with a  $\Gamma$  centered  $(2 \times 2 \times 1)$  k-point grid (Figure 1B). Electronic exchange—correlation energy was calculated using the generalized gradient approximation. Designed, optimized, norm-conserving, and nonlocal pseudopotentials generated using OPIUM (version 3.7) software are employed. The energy cutoff used was 50 Ry to expand the wave functions of the valence electrons in plane-wave basis. Additionally, we have used DFT-D3 dispersion correction to capture noncovalent interactions.

#### ASSOCIATED CONTENT

## Supporting Information

The Supporting Information is available free of charge at https://pubs.acs.org/doi/10.1021/jacs.3c08850.

Additional density functional theory calculation details and population distribution plots (PDF)

#### AUTHOR INFORMATION

#### **Corresponding Author**

Andrew M. Rappe — Department of Chemistry, University of Pennsylvania, Philadelphia, Pennsylvania 19104-6323, United States; orcid.org/0000-0003-4620-6496; Email: rappe@sas.upenn.edu

#### Authors

Sayan Banerjee – Department of Chemistry, University of Pennsylvania, Philadelphia, Pennsylvania 19104-6323, United States; ocid.org/0000-0002-8586-9236

Nathaniel Hawthorne – Department of Chemistry, Texas A&M University, College Station, Texas 77843-3255, United States

Complete contact information is available at: https://pubs.acs.org/10.1021/jacs.3c08850

#### **Notes**

The authors declare no competing financial interest.

## ■ ACKNOWLEDGMENTS

The work is supported by the NSF Center for the Mechanical Control of Chemistry under grant CHE-2023644 and CHE-2303044. S.B. acknowledges the Vagelos Institute for Energy Science and Technology for the graduate fellowship.

#### REFERENCES

- (1) Shang, W.; Zhu, X.; Liang, T.; Du, C.; Hu, L.; Li, T.; Liu, M. Chiral Reticular Self-Assembly of Achiral AIEgen into Optically Pure Metal—Organic Frameworks (MOFs) with Dual Mechano-Switchable Circularly Polarized Luminescence. *Angew. Chem., Int. Ed.* **2020**, *59*, 12811—12816.
- (2) Tu, D.; Zhang, J.; Zhang, Y.; Sung, H. H. Y.; Liu, L.; Kwok, R. T. K.; Lam, J. W. Y.; Williams, I. D.; Yan, H.; Tang, B. Z. How Do Molecular Motions Affect Structures and Properties at Molecule and Aggregate Levels? *J. Am. Chem. Soc.* **2021**, *143*, 11820–11827.
- (3) Hammes-Schiffer, S.; Benkovic, S. J. Relating Protein Motion to Catalysis. *Annu. Rev. Biochem.* **2006**, *75*, 519–541.

- (4) van Dijk, L.; Tilby, M. J.; Szpera, R.; Smith, O. A.; Bunce, H. A.; Fletcher, S. P. Molecular machines for catalysis. *Nat. Rev. Chem* **2018**, 2, 0117
- (5) Balzani, V.; Credi, A.; Raymo, F.; Stoddart, J. Artificial Molecular Machines. *Angew. Chem., Int. Ed.* **2000**, *39*, 3348–3391.
- (6) Browne, W. R.; Feringa, B. L. Making molecular machines work. *Nat. Nanotechnol.* **2006**, *1* ((1)), 25–35.
- (7) Anelli, P. L.; Spencer, N.; Stoddart, J. F. A molecular shuttle. *J. Am. Chem. Soc.* **1991**, *113*, 5131–5133.
- (8) Bissell, R. A.; Córdova, E.; Kaifer, A. E.; Stoddart, J. F. A chemically and electrochemically switchable molecular shuttle. *Nature* 1994, 369, 133–137.
- (9) Kudernac, T.; Ruangsupapichat, N.; Parschau, M.; Maciá, B.; Katsonis, N.; Harutyunyan, S. R.; Ernst, K.-H.; Feringa, B. L. Electrically driven directional motion of a four-wheeled molecule on a metal surface. *Nature* **2011**, *479*, 208–211.
- (10) Vives, G.; Tour, J. M. Synthesis of single-molecule nanocars. *Acc. Chem. Res.* **2009**, *42*, 473–487.
- (11) Von Delius, M.; Geertsema, E. M.; Leigh, D. A. A synthetic small molecule that can walk down a track. *Nat. Chem.* **2010**, *2*, 96–101
- (12) von Delius, M.; Leigh, D. A. Walking molecules. *Chem. Soc. Rev.* **2011**, *40*, 3656–3676.
- (13) Banerjee, S.; Rappe, A. M. Mechanochemical Molecular Migration on Graphene. J. Am. Chem. Soc. 2022, 144, 7181–7188.
- (14) Dong, R.; Zhang, T.; Feng, X. Interface-Assisted Synthesis of 2D Materials: Trend and Challenges. *Chem. Rev.* **2018**, *118*, 6189–6235.
- (15) Huang, L.; Hu, Z.; Jin, H.; Wu, J.; Liu, K.; Xu, Z.; Wan, J.; Zhou, H.; Duan, J.; Hu, B.; Zhou, J. Salt-Assisted Synthesis of 2D Materials. *Adv. Funct. Mater.* **2020**, *30*, 1908486.
- (16) Zhou, J.; Lin, J.; Huang, X.; Zhou, Y.; Chen, Y.; Xia, J.; Wang, H.; Xie, Y.; Yu, H.; Lei, J.; et al. A library of atomically thin metal chalcogenides. *Nature* **2018**, *556*, 355–359.
- (17) Novoselov, K. S.; Geim, A. K.; Morozov, S. V.; Jiang, D.; Zhang, Y.; Dubonos, S. V.; Grigorieva, I. V.; Firsov, A. A. Electric Field Effect in Atomically Thin Carbon Films. *Science* **2004**, *306*, 666–669.
- (18) Lin, Z.; McCreary, A.; Briggs, N.; Subramanian, S.; Zhang, K.; Sun, Y.; Li, X.; Borys, N. J.; Yuan, H.; Fullerton-Shirey, S. K.; et al. 2D materials advances: from large scale synthesis and controlled heterostructures to improved characterization techniques, defects and applications. 2D Mater. 2016, 3, 042001.
- (19) Mas-Ballesté, R.; Gómez-Navarro, C.; Gómez-Herrero, J.; Zamora, F. 2D materials: to graphene and beyond. *Nanoscale* **2011**, *3*, 20–30.
- (20) Gupta, A.; Sakthivel, T.; Seal, S. Recent development in 2D materials beyond graphene. *Prog. Mater. Sci.* **2015**, *73*, 44–126.
- (21) Bernardi, M.; Palummo, M.; Grossman, J. C. Extraordinary Sunlight Absorption and One Nanometer Thick Photovoltaics Using Two-Dimensional Monolayer Materials. *Nano Lett.* **2013**, *13*, 3664–3670.
- (22) He, M.; Swager, T. M. Aryl Migration on Graphene. *J. Am. Chem. Soc.* **2020**, *142*, 17876–17880.
- (23) Wu, Q.; Wu, Y.; Hao, Y.; Geng, J.; Charlton, M.; Chen, S.; Ren, Y.; Ji, H.; Li, H.; Boukhvalov, D. W.; et al. Selective surface functionalization at regions of high local curvature in graphene. *Chem. Commun.* **2013**, *49*, 677–679.
- (24) Boukhvalov, D. W.; Katsnelson, M. I. Enhancement of chemical activity in corrugated graphene. *J. Phys. Chem. C* **2009**, *113*, 14176–14178.
- (25) Deng, S.; Rhee, D.; Lee, W.-K.; Che, S.; Keisham, B.; Berry, V.; Odom, T. W. Graphene wrinkles enable spatially defined chemistry. *Nano Lett.* **2019**, *19*, 5640–5646.
- (26) Bissett, M. A.; Konabe, S.; Okada, S.; Tsuji, M.; Ago, H. Enhanced Chemical Reactivity of Graphene Induced by Mechanical Strain. *ACS Nano* **2013**, *7*, 10335–10343.
- (27) Nguyen, M.-T. An ab initio study of oxygen on strained graphene. J. Phys.: Condens. Matter 2013, 25, 395301.

- (28) Qu, Y.; Ke, Y.; Shao, Y.; Chen, W.; Kwok, C. T.; Shi, X.; Pan, H. Effect of Curvature on the Hydrogen Evolution Reaction of Graphene. *J. Phys. Chem. C* **2018**, *122*, 25331–25338.
- (29) Shen, Y.; Dai, E.; Liu, X.; Pan, W.; Yang, H.; Xiong, B.; Zerulla, D. Curvature analysis of single layer graphene on the basis of extreme low-frequency Raman spectroscopy. *Appl. Phys. Lett.* **2019**, *114*, 161907.
- (30) Hawthorne, N.; Banerjee, S.; Moore, Q.; Rappe, A. M.; Batteas, J. D. Studies of the Reactivity of Graphene Driven by Mechanical Distortions. *J. Phys. Chem. C* **2022**, *126*, 17569–17578.
- (31) Ribas-Arino, J.; Marx, D. Covalent Mechanochemistry: Theoretical Concepts and Computational Tools with Applications to Molecular Nanomechanics. *Chem. Rev.* **2012**, *112*, 5412–5487.
- (32) Do, J.-L.; Friščić, T. Mechanochemistry: A Force of Synthesis. ACS Cent. Sci. 2017, 3, 13–19.
- (33) Beyer, M. K.; Clausen-Schaumann, H. Mechanochemistry: The Mechanical Activation of Covalent Bonds. *Chem. Rev.* **2005**, *105*, 2921–2948.
- (34) Garcia-Manyes, S.; Beedle, A. E. M. Steering chemical reactions with force. *Nat. Rev. Chem* **2017**, *1*, 0083–116.
- (35) Andrews, J. L.; Stein, P.; Santos, D. A.; Chalker, C. J.; De Jesus, L. R.; Davidson, R. D.; Gross, M. A.; Pharr, M.; Batteas, J. D.; Xu, B.-X.; Banerjee, S. Curvature-Induced Modification of Mechano-Electrochemical Coupling and Nucleation Kinetics in a Cathode Material. *Matter* **2020**, *3*, 1754–1773.
- (36) Hickenboth, C. R.; Moore, J. S.; White, S. R.; Sottos, N. R.; Baudry, J.; Wilson, S. R. Biasing reaction pathways with mechanical force. *Nature* **2007**, 446, 423–427.
- (37) Wang, J.; Kouznetsova, T. B.; Niu, Z.; Ong, M. T.; Klukovich, H. M.; Rheingold, A. L.; Martinez, T. J.; Craig, S. L. Inducing and quantifying forbidden reactivity with single-molecule polymer mechanochemistry. *Nat. Chem.* **2015**, *7*, 323–327.
- (38) Han, X.; Bian, S.; Liang, Y.; Houk, K. N.; Braunschweig, A. B. Reactions in Elastomeric Nanoreactors Reveal the Role of Force on the Kinetics of the Huisgen Reaction on Surfaces. *J. Am. Chem. Soc.* **2014**, *136*, 10553–10556.
- (39) Yang, F.; Yang, J.; Qi, Y.; de Boer, M. P.; Carpick, R. W.; Rappe, A. M.; Srolovitz, D. J. Mechanochemical Effects of Adsorbates at Nanoelectromechanical Switch Contacts. *ACS Appl. Mater. Interfaces* **2019**, *11*, 39238–39247.
- (40) Yang, J.; Qi, Y.; Kim, H. D.; Rappe, A. M. Mechanism of Benzene Tribopolymerization on the  $RuO_2(110)$  Surface. *Phys. Rev. Appl.* **2018**, *9*, 044038.
- (41) Qi, Y.; Yang, J.; Rappe, A. M. Theoretical Modeling of Tribochemical Reaction on Pt and Au Contacts: Mechanical Load and Catalysis. ACS Appl. Mater. Interfaces 2016, 8, 7529–7535.
- (42) Chen, B.; Crespi, V. H.; Hoffmann, R. Theoretical Studies of Furan and Thiophene Nanothreads: Structures, Cycloaddition Barriers, and Activation Volumes. *J. Am. Chem. Soc.* **2022**, *144*, 9044–9056.
- (43) Biswas, S.; Banerjee, S.; Shlain, M. A.; Bardin, A. A.; Ulijn, R. V.; Nannenga, B. L.; Rappe, A. M.; Braunschweig, A. B. Photomechanochemical control over stereoselectivity in the [2 + 2] photodimerization of acenaphthylene. *Faraday Discuss.* **2023**, 241, 266–277.
- (44) Banerjee, S.; Rappe, A. M. Mechanochemical Molecular Motion Using Noncovalent Interactions on Graphene and Its Application to Tailoring the Adsorption Energetics. *ACS Mater. Lett.* **2023**, *5*, 574–579.
- (45) Chua, C. K.; Pumera, M. Covalent chemistry on graphene. Chem. Soc. Rev. 2013, 42, 3222–3233.
- (46) Jin, B.; Shen, J.; Peng, R.; Chen, C.; Zhang, Q.; Wang, X.; Chu, S. DMSO: An Efficient Catalyst for the Cyclopropanation of C<sub>60</sub>, C<sub>70</sub>, SWNTs, and Graphene through the Bingel Reaction. *Ind. Eng. Chem. Res.* **2015**. *54*. 2879–2885.
- (47) Baachaoui, S.; Aldulaijan, S.; Raouafi, F.; Besbes, R.; Sementa, L.; Fortunelli, A.; Raouafi, N.; Dhouib, A. Pristine graphene covalent functionalization with aromatic aziridines and their application in the

- sensing of volatile amines-an ab initio investigation. RSC Adv. 2021, 11, 7070-7077.
- (48) Suggs, K.; Reuven, D.; Wang, X.-Q. Electronic Properties of Cycloaddition-Functionalized Graphene. *J. Phys. Chem. C* **2011**, *115*, 3313—3317
- (49) Kutana, A.; Giapis, K. P. First-Principles Study of Chemisorption of Oxygen and Aziridine on Graphitic Nanostructures. *J. Phys. Chem. C* **2009**, *113*, 14721–14726.
- (50) Yang, X.; Chen, F.; Kim, M. A.; Liu, H.; Wolf, L. M.; Yan, M. On the Reactivity Enhancement of Graphene by Metallic Substrates towards Aryl Nitrene Cycloadditions. *Chem.—Eur. J.* **2021**, 27, 7887—7896
- (51) Liu, L.-H.; Lerner, M. M.; Yan, M. Derivitization of Pristine Graphene with Well-Defined Chemical Functionalities. *Nano Lett.* **2010**, *10*, 3754–3756.
- (52) Plachinda, P.; Evans, D.; Solanki, R. Electrical conductivity of PFPA functionalized graphene. *Solid-State Electron.* **2013**, *79*, 262–267.
- (53) Negrito, M.; Elinski, M. B.; Hawthorne, N.; Pedley, M. P.; Han, M.; Sheldon, M.; Espinosa-Marzal, R. M.; Batteas, J. D. Using Patterned Self-Assembled Monolayers to Tune Graphene—Substrate Interactions. *Langmuir* **2021**, *37*, 9996—10005.
- (54) Park, J.; Yan, M. Covalent functionalization of graphene with reactive intermediates. *Acc. Chem. Res.* **2013**, *46*, 181–189.
- (55) Johns, J. E.; Hersam, M. C. Atomic covalent functionalization of graphene. *Acc. Chem. Res.* **2013**, *46*, 77–86.
- (56) Quintana, M.; Spyrou, K.; Grzelczak, M.; Browne, W. R.; Rudolf, P.; Prato, M. Functionalization of graphene via 1, 3-dipolar cycloaddition. *ACS Nano* **2010**, *4*, 3527–3533.
- (57) Gao, T.; Xie, S.; Gao, Y.; Liu, M.; Chen, Y.; Zhang, Y.; Liu, Z. Growth and Atomic-Scale Characterizations of Graphene on Multifaceted Textured Pt Foils Prepared by Chemical Vapor Deposition. *ACS Nano* **2011**, *5*, 9194–9201.
- (58) Zhang, Y.; Gao, T.; Gao, Y.; Xie, S.; Ji, Q.; Yan, K.; Peng, H.; Liu, Z. Defect-like Structures of Graphene on Copper Foils for Strain Relief Investigated by High-Resolution Scanning Tunneling Microscopy. *ACS Nano* **2011**, *5*, 4014–4022.
- (59) Ishigami, M.; Chen, J. H.; Cullen, W. G.; Fuhrer, M. S.; Williams, E. D. Atomic Structure of Graphene on SiO<sub>2</sub>. *Nano Lett.* **2007**, *7*, 1643–1648.
- (60) Venema, L. C.; Meunier, V.; Lambin, P.; Dekker, C. Atomic structure of carbon nanotubes from scanning tunneling microscopy. *Phys. Rev. B* **2000**, *61*, 2991–2996.
- (61) Yan, W.; He, W.-Y.; Chu, Z.-D.; Liu, M.; Meng, L.; Dou, R.-F.; Zhang, Y.; Liu, Z.; Nie, J.-C.; He, L. Strain and curvature induced evolution of electronic band structures in twisted graphene bilayer. *Nat. Commun.* **2013**, *4*, 2159.
- (62) Meyer, J. C.; Geim, A. K.; Katsnelson, M. I.; Novoselov, K. S.; Booth, T. J.; Roth, S. The structure of suspended graphene sheets. *Nature* **2007**, *446*, 60–63.
- (63) Thompson-Flagg, R. C.; Moura, M. J.; Marder, M. Rippling of graphene. *Europhys. Lett.* **2009**, 85, 46002.
- (64) Falvo, M. R.; Clary, G. J.; Taylor, R. M.; Chi, V.; Brooks, F. P.; Washburn, S.; Superfine, R. Bending and buckling of carbon nanotubes under large strain. *Nature* **1997**, 389, 582–584.
- (65) Cheung, C. L.; Hafner, J. H.; Lieber, C. M. Carbon nanotube atomic force microscopy tips: Direct growth by chemical vapor deposition and application to high-resolution imaging. *Proc. Natl. Acad. Sci. U.S.A.* **2000**, *97*, 3809–3813.
- (66) Imadate, K.; Hirahara, K. Experimental determination of the diameter-dependent wettability of carbon nanotubes as studied using atomic force microscopy. *Phys. Chem. Chem. Phys.* **2018**, 20, 26979—26985.
- (67) Gotovac, S.; Honda, H.; Hattori, Y.; Takahashi, K.; Kanoh, H.; Kaneko, K. Effect of Nanoscale Curvature of Single-Walled Carbon Nanotubes on Adsorption of Polycyclic Aromatic Hydrocarbons. *Nano Lett.* **2007**, *7*, 583–587.
- (68) Darlington, T. P.; Carmesin, C.; Florian, M.; Yanev, E.; Ajayi, O.; Ardelean, J.; Rhodes, D. A.; Ghiotto, A.; Krayev, A.; Watanabe, K.;

- et al. Imaging strain-localized excitons in nanoscale bubbles of monolayer WSe<sub>2</sub> at room temperature. *Nat. Nanotechnol.* **2020**, *15*, 854–860.
- (69) Haddon, R. C. Chemistry of the Fullerenes: The Manifestation of Strain in a Class of Continuous Aromatic Molecules. *Science* **1993**, 261, 1545–1550.
- (70) Haddon, R. C. Hybridization and the orientation and alignment of  $\pi$ -orbitals in nonplanar conjugated organic molecules:  $\pi$ -orbital axis vector analysis (POAV2). *J. Am. Chem. Soc.* **1986**, *108*, 2837–2842.
- (71) Haddon, R. C. Pyramidalization: geometrical interpretation of the  $\pi$ -orbital axis vector in three dimensions. *J. Phys. Chem.* **1987**, *91*, 3719–3720.
- (72) Haddon, R. C. Rehybridization and  $\pi$ -orbital overlap in nonplanar conjugated organic molecules:  $\pi$ -orbital axis vector (POAV) analysis and three-dimensional Hueckel molecular orbital (3D-HMO) theory. *J. Am. Chem. Soc.* **1987**, *109*, 1676–1685.
- (73) Wehling, T. O.; Grundkötter-Stock, B.; Aradi, B.; Frauenheim, T.; Niehaus, T. Charge-doping-induced phase transitions in hydrogenated and fluorinated graphene. *Phys. Rev. B* **2014**, *90*, 085422.
- (74) Banerjee, S.; Kakekhani, A.; Wexler, R. B.; Rappe, A. M. Relationship between the Surface Reconstruction of Nickel Phosphides and Their Activity toward the Hydrogen Evolution Reaction. ACS Catal. 2023, 13, 4611–4621.
- (75) Zholdassov, Y. S.; Yuan, L.; Garcia, S. R.; Kwok, R. W.; Boscoboinik, A.; Valles, D. J.; Marianski, M.; Martini, A.; Carpick, R. W.; Braunschweig, A. B. Acceleration of Diels-Alder reactions by mechanical distortion. *Science* **2023**, *380*, 1053–1058.
- (76) Giannozzi, P.; Baroni, S.; Bonini, N.; Calandra, M.; Car, R.; Cavazzoni, C.; Ceresoli, D.; Chiarotti, G. L.; Cococcioni, M.; Dabo, I.; et al. QUANTUM ESPRESSO: A Modular and Open-source Software Project for Quantum Simulations of Materials. *J. Phys.: Condens. Matter* **2009**, *21*, 395502.
- (77) Henkelman, G.; Uberuaga, B. P.; Jónsson, H. A Climbing Image Nudged Elastic Band Method for Finding Saddle Points and Minimum Energy Paths. *J. Chem. Phys.* **2000**, *113*, 9901–9904.
- (78) Perdew, J. P.; Burke, K.; Ernzerhof, M. Generalized Gradient Approximation Made Simple. *Phys. Rev. Lett.* **1996**, 77, 3865–3868.
- (79) Rappe, A. M.; Rabe, K. M.; Kaxiras, E.; Joannopoulos, J. D. Optimized Pseudopotentials. *Phys. Rev. B* **1990**, *41*, 1227–1230.
- (80) Ramer, N. J.; Rappe, A. M. Designed Nonlocal Pseudopotentials for Enhanced Transferability. *Phys. Rev. B* **1999**, *59*, 12471–12478.
- (81) Grimme, S.; Antony, J.; Ehrlich, S.; Krieg, H. A consistent and accurate ab initio parametrization of density functional dispersion correction (DFT-D) for the 94 elements H-Pu. *J. Chem. Phys.* **2010**, 132, 154104.